www.sciencemag.org/cgi/content/full/330/6003/479/DC1

Supporting Online Material for

Diviner Lunar Radiometer Observations of Cold Traps in the Moon's South Polar Region

David A. Paige,* Matthew A. Siegler, Jo Ann Zhang, Paul. O. Hayne, Emily J. Foote, Kristen A. Bennett, Ashwin R. Vasavada, Benjamin T. Greenhagen, John. T. Schofield, Daniel J. McCleese, Marc C. Foote, Eric DeJong, Bruce G. Bills, Wayne Hartford, Bruce C. Murray, Carlton C. Allen, Kelly Snook, Laurence A. Soderblom, Simon Calcutt, Fredric W. Taylor, Neil E. Bowles, Joshua L. Bandfield, Richard Elphic, Rebecca Ghent, Timothy D. Glotch, Michael. B. Wyatt, Paul. G. Lucey

*To whom correspondence should be addressed. E-mail: dap@moon.ucla.edu

Published 22 October 2010, *Science* **330**, 479 (2010)
DOI: 10.1126/science.1187726

This PDF file includes:

Materials and Methods
Figs. S1 to S7
References

Other Supporting Online Material for this manuscript includes the following:
(available at www.sciencemag.org/cgi/content/full/330/6003/479/DC1)

High-resolution versions of Fig. 1 from the main paper and figs. S3 and S7 from the Supporting Online Material (PNG format).

Supporting Online Material for

Diviner Observations of Cold Traps in the Lunar South Polar Region: Spatial Distribution and Temperature

David A. Paige[1], Matthew A. Siegler[1], Jo Ann Zhang[1], Paul. O. Hayne[1], Emily J. Foote[1], Kristen A. Bennett[1], Ashwin R. Vasavada[2], Benjamin T. Greenhagen[2], John. T. Schofield[2], Daniel J. McCleese[2], Marc C. Foote[2], Eric DeJong[2], Bruce G. Bills[2], Wayne Hartford[2], Bruce. C. Murray[3], Carlton C. Allen[4], Kelly Snook[5], Laurence A. Soderblom[6], Simon Calcutt[7], Fredric W. Taylor[7], Neil E. Bowles[7], Joshua L. Bandfield[8], Richard Elphic[9], Rebecca Ghent[10], Timothy D. Glotch[11], Michael. B. Wyatt[12] and Paul. G. Lucey[13].

[1]Department of Earth and Space Sciences, UCLA
[2]Jet Propulsion Laboratory, California Institute of Technology
[3]California Institute of Technology
[4]NASA Johnson Space Center
[5]NASA Goddard Space Flight Center
[6]US Geologic Survey
[7]Oxford University
[8]University of Washington
[9]NASA Ames Research Center
[10]University of Toronto
[11]State University of New York, Stony Brook
[12]Brown University
[13]University of Hawaii

Correspondence should be directed to:
David A. Paige
Dept. of Earth and Space Sciences
University of California, Los Angeles
595 Charles E. Young Drive East
Los Angeles, Ca 90049
Phone: 310-825-4268
Fax: 310-825-2779
Email: dap@moon.ucla.edu

Revised 6/26/10

Description of the Diviner Instrument

The Diviner instrument is described in Paige et al. (2009). The in-flight performance of the instrument has been consistent with pre-flight calibration measurements.

Bolometric Brightness Temperature

The bolometric brightness temperature T_{BOL} is a measure of the spectrally integrated flux of infrared radiation emerging from the surface. It is computed from the measured brightness temperatures in Diviner infrared channels as follows:

$$\sigma T_{BOL}^4 = \sum_{i=3}^{9} \sigma T_i^4 f(T_i, \lambda_1, \lambda_2)$$

Where T_i is the average radiance-weighted measured brightness temperature for a region in Diviner channel *i*, and:

$$f(T_i, \lambda_1, \lambda_2) = \frac{\int_{\lambda_1}^{\lambda_2} B(\lambda, T)\, d\lambda}{\int_0^{\infty} B(\lambda, T)\, d\lambda}$$

Where $B(\lambda, T)$ is the Planck function of wavelength λ and temperature *T*. T_{BOL} is computed using the following values for λ_1 and λ_2:

Diviner Channel	3	4	5	6	7	8	9
λ_1(µm)	0	8.075	8.40	13	25	50	100
λ_2(µm)	8.075	8.40	13	25	50	100	1000
λ_{min}(µm)	7.55	8.10	8.38	13	25	50	100
λ_{max}(µm)	8.05	8.40	8.68	23	41	100	400
T_{min}(K)	190	190	180	95	60	40	-

Where λ_{min} and λ_{max}(μm) are the measured minimum and maximum wavelengths of the spectral passbands of the Diviner channels, and T_{min} is our estimate for the minimum detectable temperature in each channel while maintaining a high signal to noise ratio. If the radiance weighted average brightness temperature for a region drops below T_{min}, then the brightness temperature in that channel is assumed to be equal to the brightness temperature in the next longest wavelength channel with a brightness temperature higher than its respective T_{min}.

Significance of the Bolometric Brightness Temperature

We use T_{BOL} rather than the brightness temperatures in the individual Diviner spectral channels because is T_{BOL} is more directly related to the heat balance of the surface. In general, the Diviner footprint may contain a distribution of temperatures and spectral emissivities that can result in a complex scene that exhibits large differences between measured brightness temperatures at different wavelengths. This is especially true for directly illuminated surfaces at high solar-zenith angles where local topography creates shadows. However, regardless of the complexity of the scene, if the region within a Diviner footprint is in a state of radiative equilibrium, then there will be a balance between the absorbed flux of solar radiation and the emitted flux of infrared radiation:

$$\sigma T_{BOL}^4 = \pi \int_0^\infty \varepsilon(\lambda) B(\lambda, T_s) d\lambda = S_0 (1 - A)$$

Where $\varepsilon(\lambda)$ is the emissivity of the surface as a function of wavelength, T_s is the surface kinetic temperature, S_0 is the incident flux of solar radiation and A is the solar spectrum averaged surface albedo. Therefore, for illuminated surfaces that are close to being in a state of radiative equilibrium, measuring T_{BOL} makes it possible to derive a self-consistent albedo of the surface in a straightforward manner. Furthermore, since T_{BOL} is a measure of the spectrally integrated infrared flux leaving the surface, it is directly relevant to determining infrared heating rates in the shadowed regions of impact craters, where absorbed infrared radiation from warmer crater walls dominates the heat balance.

Employing T_{BOL} also vastly simplifies the comparison between Diviner data and existing thermal models because it makes it possible to sidestep many issues relating to quantifying parameters such as the spectral emissivity of the surface or the distribution of slopes within a Diviner footprint.

Diviner Temperature Maps (Fig. 1A-B)

The Diviner temperature maps shown in Figures 1A-B have been produced in a manner that enables precise comparison with models. The following procedures were employed:

1. The Diviner radiances in all channels were selected by date, local time (6-18 hrs local time for the daytime map and 0-6 and 18-24 hours local time for the nighttime map), and by viewing geometry (nadir pushbroom mode only) . Most of the data from regions equatorward of 88° south were acquired within a two-hour local time window.
2. The surface location of each measurement was ray-traced onto a three-dimensional ~500 meter triangular mesh (which will be described later in the Model Description section) and the radiances that fell within each triangle were binned and averaged
3. The radiances were converted to brightness temperatures and T_{BOL} was computed for each triangle
4. The resulting maps were plotted using a polar stereographic projection assuming a spherical planet with a radius of 1737.4 km.

Gaps in the maps in Figures 1A-B are due to routine Diviner space and internal blackbody calibrations, and off-nadir slews by the LRO spacecraft. The warm regions in the nighttime map shown in Figure 1B are due to the presence of areas of high topographic relief close to the pole that receive direct illumination despite the local time constraint.

Surface Emissivity and Surface Temperatures

The maps of bolometric measured brightness temperature make no specific assumptions regarding the spectral emissivity of the surface. However, the interpretation of Diviner data in terms of actual surface temperature is desirable in order to quantify subsurface heat conduction or the stability of volatile species. Figures S1A-B show data density cross plots of Diviner brightness temperatures in channels 7 vs. 9, and channels 8 vs. 9 for the daytime data shown in Figure 1A. The plots show that the data are separated into to two distinct families. The high temperature family of points consists of directly illuminated regions that have an anisothermal distribution of temperatures at length scales smaller than a Diviner footprint. These regions exhibit higher brightness temperatures at shorter wavelengths due to the non-linearity of the Planck function. The effects of anisothermality are most pronounced for the lowest temperature populations in this family, which are illuminated at the highest incidence angles. The low temperature family of points consist of the cryogenic regions that do not receive direct sunlight. The angular distribution of radiative heat sources in these regions is much wider than in the directly illuminated regions, and surface temperatures are more spatially uniform. Figures S1A-B also show calculated brightness temperatures for the case where the surface emissivity in one channel is unity, and the other channel is less than unity. We interpret the relatively good agreement between the measured brightness temperatures in channels 7, 8 and 9 in the cryogenic regions as consistent with high spectral emissivities in all three channels. As a consequence, we have chosen to interpret measured bolometric brightness temperatures in these regions as equal to the surface temperature, and have assumed that the spectral emissivity of the surface is unity in our model calculations.

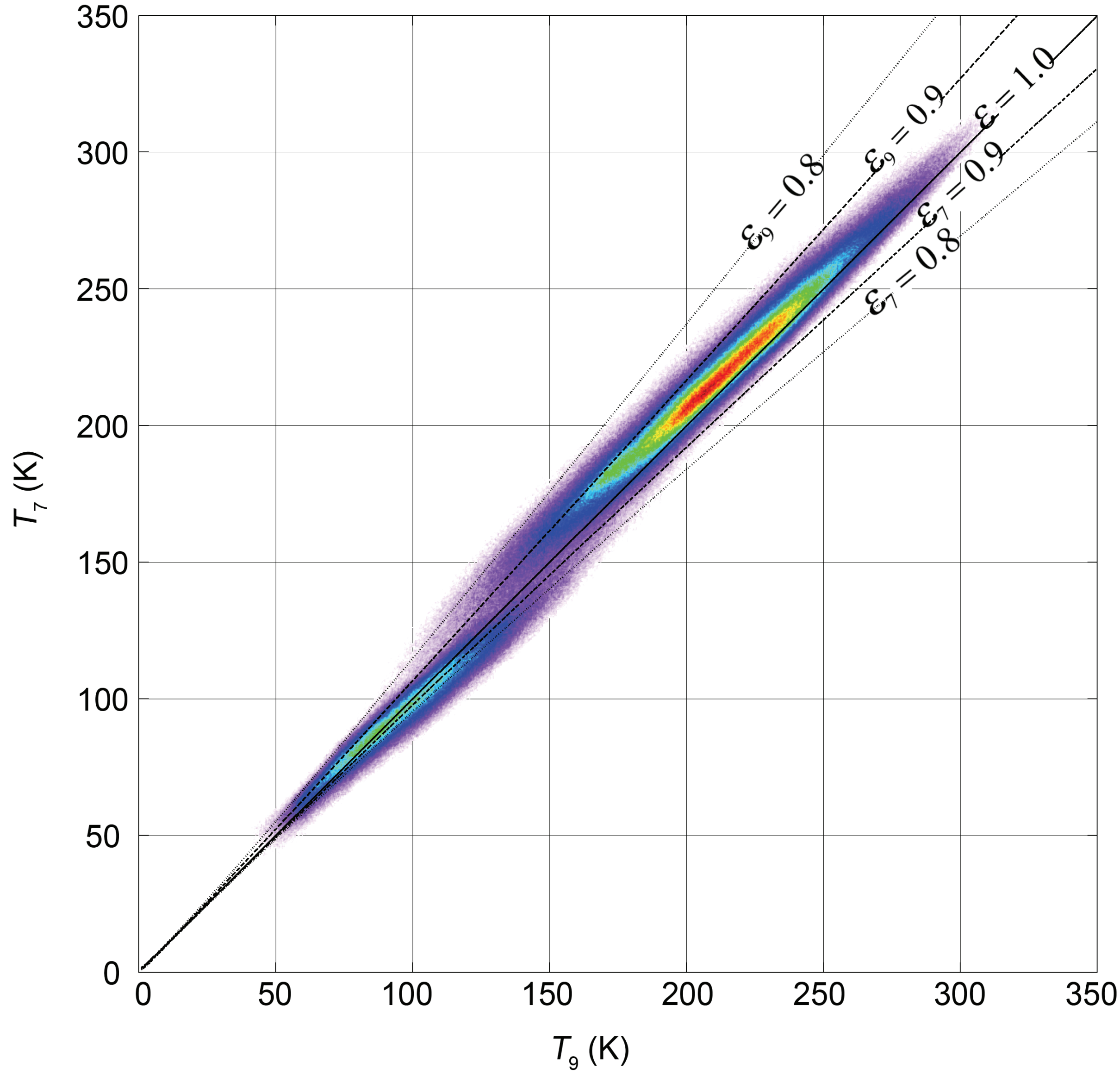

Figure S1-A. Data density cross-plot of measured Diviner south polar daytime brightness temperatures in Channel 7 (25-41 µm) vs Channel 9 (100-400 µm).

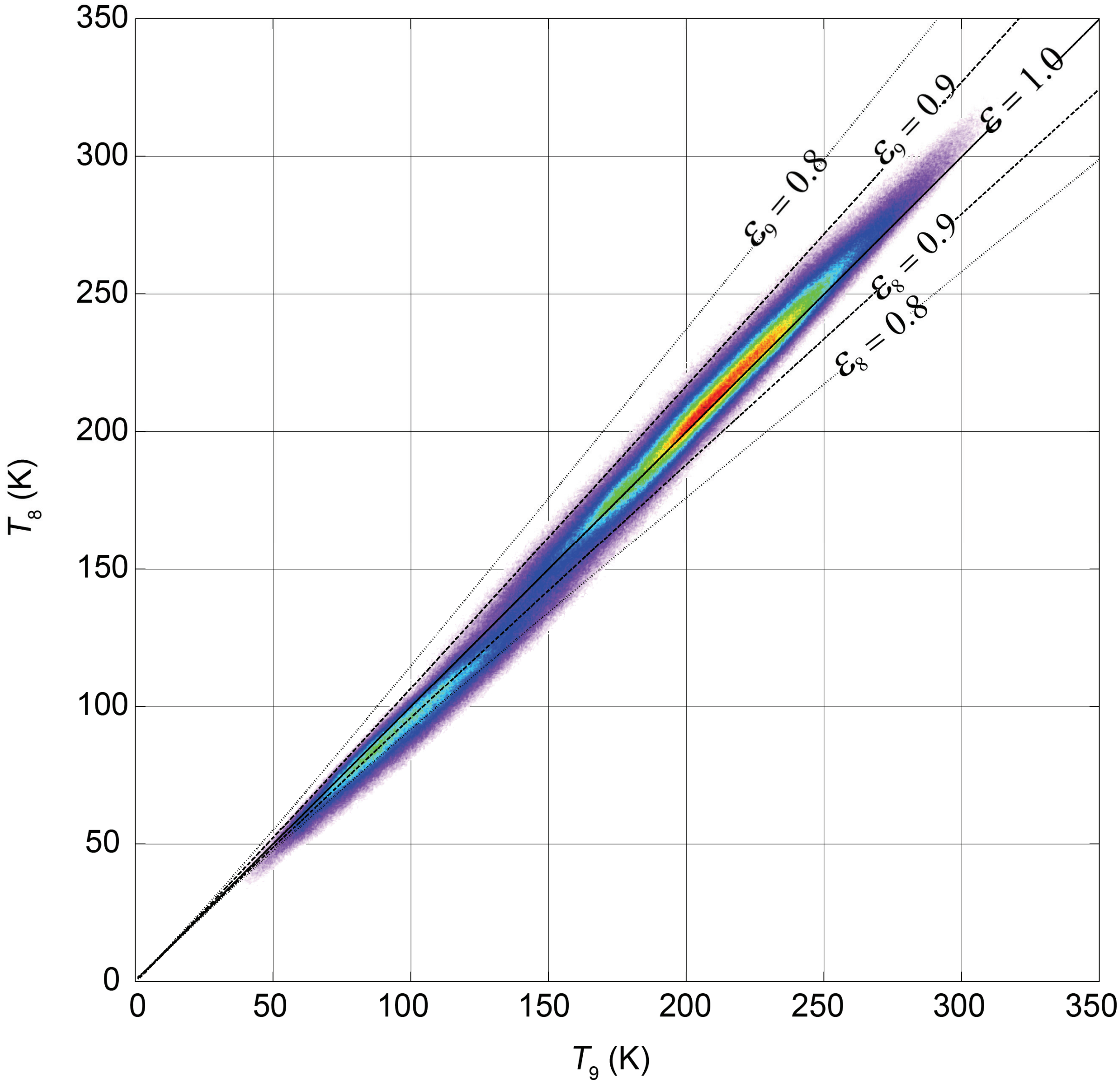

Fig. S1-B. Data density cross-plot of measured Diviner south polar daytime brightness temperatures in Channel 8 (50-100 μm) vs Channel 9 (100-400 μm).

Thermal Model Description

The thermal model employed in this study is intended to be the simplest model that can reproduce the major features of the Diviner south polar observations. The model uses a generic set of input parameters and only modest effort has gone into tuning.

Triangular Mesh

The model calculations are performed on a triangular mesh based on the Kaguya LALT laser altimeter dataset (Araki et. al., 2009). The mesh vertices were determined by sampling the Lunar Global Topographic Data as Time Series provided on the online SELENE Data Archive. The mesh covers the mapped area in Figure 1 and consists of 2,880,000 triangles, each with edge dimensions of approximately 500 meters.

Sun and Earth Models and Ephemeris

The sun is also modeled as a triangular mesh consisting of 32 visible triangles whose radiance falls off with distance from the center of the sun according to the solar limb darkening curve (Negi, et al 1985). The Earth is modeled as a geodesic spherical mesh consisting of 80 triangles with solar spectrum albedo and bolometric thermal emission properties taken from the results of earth radiation budget observations (Vonder Haar and Soumi, 1969) The location and distance of the sun and earth, as well as the spin pole orientation of the Earth as a function of time is determined using the DE421 JPL Planetary Ephemeris.

Direct Solar Heating

Direct solar heating of the surface is computed by ray tracing from the center of each moon triangle to the center of each sun triangle to determine the resulting flux of direct incident solar radiation. Direct heating of the surface by solar earthshine is determined by computing the incident solar flux on each earth triangle and then ray tracing from the center of each moon triangle to the center of each earth triangle to compute the flux of solar energy reflected by the earth, which depends of earth phase and earth spin pole orientation. The only free parameter in this calculation is A, the solar spectrum average albedo of the lunar surface. We find that computed surface temperatures using a fixed value A=0.2 yields an excellent fit to the Diviner observations in directly solar illuminated areas in the south polar region. As a demonstration of the plausibility of this value for the albedo, we show in Figure S2 that it is consistent with Clementine measurements of the average normal reflectance of lunar highlands terrains at 750 nm.

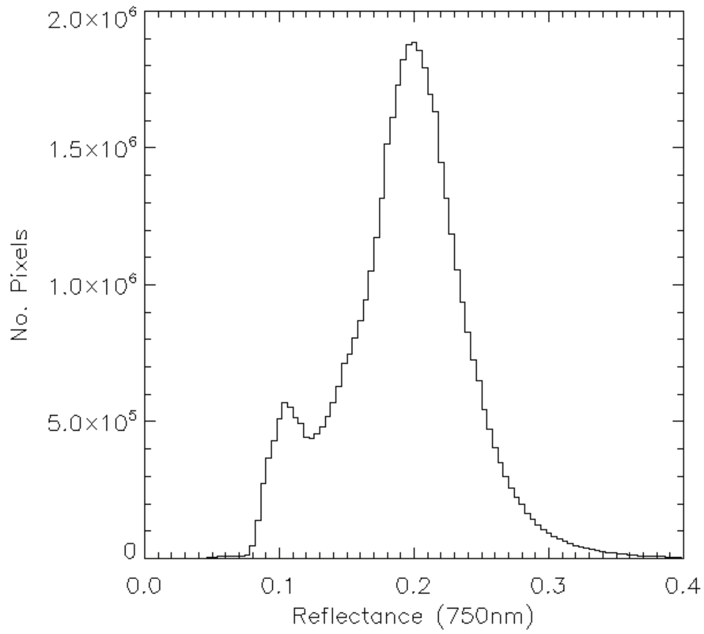

Figure S2. Histogram of Clementine normal albedos at 750 nm wavelength. The histogram of reflectance values was derived from a mosaic of digital image of the Moon obtained by the Clementine lunar orbiter prepared by the USGS (Isbell et al. 1999) and downloaded from the USGS. The data obtained at a range of incidence and emission angle were corrected using the Mcewen (1996) lunar photometric normalization function, and then scaled at the Apollo 16 landing site to laboratory measurements of Apollo Sample 62231 as representative of that location, and measured at an incidence angle of 30° and an emission angle of 0°. The data used cover all longitudes, and latitudes from -70 degrees to +70 degrees, were originally sampled at 1 km resolution in simple cylindrical projection. To produce the histogram the data were resampled to Lambert Equal Area projection to preserve the areal abundances over all latitudes. The absolute reflectance values are scaled to the reflectance of a lunar highlands soil at a location near the Apollo 16 landing site (Isbell et al. 1999). The histogram is sampled in reflectance bin widths of .04 reflectance units

Direct Infrared Heating

Direct infrared heating of the surface by infrared earthshine is calculated by ray tracing from the center of each moon triangle to the center of each earth triangle to compute the flux of emitted infrared energy by the earth incident on the moon. The flux of infrared earthshine is roughly 60% as great as the flux of solar earthshine at full earth.

Indirect Solar Heating

Indirect solar heating is calculated using a recursive scatter gather approach. When the model is initialized, a set of 2304 rays are projected from the centers of each triangle to determine the visibility of other triangles in the mesh. During each timestep, the direct solar energy not absorbed by each triangle is scattered isotropically along a set of rays to other visible triangles in the mesh. The solar heating calculations employ three generations of radiation scattering and gathering (three bounces) to ensure penetration of scattered solar radiation into doubly and triply shadowed regions.

Infrared Emission and Indirect Heating

Infrared emission and indirect heating are computed in a manner analogous to that used for solar heating, assuming that the surface is an isotropic grey-body emitter and absorber with constant emissivity as a function of wavelength. The bolometric brightness temperature T_{bol} is computed as: $\sigma T_{bol}^4 = \varepsilon\sigma T_s^4 + (1-\varepsilon)F_{IR}$ where ε is the emissivity of the surface, T_{s} is the surface temperature and F_{IR} is flux of incident infrared radiation from other triangles in the mesh. For the calculations presented here, we assume that the surface emissivity is unity, and therefore only one generation of scattering and gathering is required.

Subsurface Thermal Model

A one-dimensional thermal model is used to calculate surface and subsurface temperatures for each triangle in the mesh. We used the two-layer thermal model parameters described in Vasavada et al. (1999) as a starting point for our thermal model input parameters, which assume a temperature-dependent heat capacities at all depths, and a 2 cm low-density surface layer with "TOP" temperature-dependent thermal properties overlaying deeper, higher-density layer with "BOT" temperature-dependent thermal properties at depths of greater than 2 cm (see Vasavada et al., 1999). Similar models have been used to reproduce in-situ temperature measurements as a function of depth at the Apollo 15 and 17 landing sites (Langseth et al 1976, Keihm 1984). After some experimentation, we found that more satisfactory fits to the Diviner nighttime observations in the south polar region could be obtained if the thermal conductivity of the TOP layer was reduced by a factor of two. The following table shows the spatially uniform thermal parameters used for the thermal model calculations in this paper:

Depth Range	k_c (W m^{-1} K^{-1})	χ	P (kg m^{-3})
0 – 2 cm	0.000461	1.48	1300
> 2 cm	0.0093	0.073	1800

Where the temperature-dependent thermal conductivity of the soil is parameterized as $k = k_c[1 + \chi(T/350)^3]$. We do not consider these thermal properties to be unique, and other combinations of parameters can provide equally good fits. The fact that we require a lower thermal conductivity for the upper soil layer may be due to the differences between the thermal properties of the highlands regolith material that covers the south polar region compared to the maria regolith material at the Apollo 15 and 17 sites. Lateral heat conduction is ignored in these calculations, which is appropriate given the length scales involved and the thermal diffusivity of the lunar regolith. We assume a fixed heat flow rate of 0.016 Wm^{-2} for all calculations.

Model Initialization and Time Steps

The model employs a one Earth day time step for solar and infrared heating calculations, and a 1/52 Earth day time step for thermal conduction calculations. To achieve good interannual convergence, we have found it sufficient to initialize subsurface temperatures at 80K, and then run the model to a depth of 20 cm depths for approximately 6 years, and then use the resulting annual average temperatures to reinitialize the model to a depth of 2.8 m, and then run it for an additional 6 years.

Model Simulations of Diviner Data

We have used the model to create simulated Diviner bolometric temperature maps using the following procedure:

1. A thermal model calculation is performed on the triangular mesh and a database of model-calculated bolometric brightness temperatures is created for each triangle at a set of discrete Julian Dates that span the observation period is created
2. The surface location of each Diviner channel 9 measurement is ray-traced onto the same triangular mesh used for the model calculations and a time-interpolated model-calculated bolometric radiance is computed for each measurement

3. The time-interpolated bolometric radiances that fall within each triangle are averaged in a manner analogous to that used for the data to produce simulated model-calculated bolometric temperatures

The resulting maps for the Diviner data used in Figures 1A-B are shown in Figures S3A-B. Histograms of the measured and model-calculated data are shown in Figure 2A. Scatter plots of the model-calculated surface temperatures vs. the Diviner bolometric temperature observations are shown in Figures S4A-B.

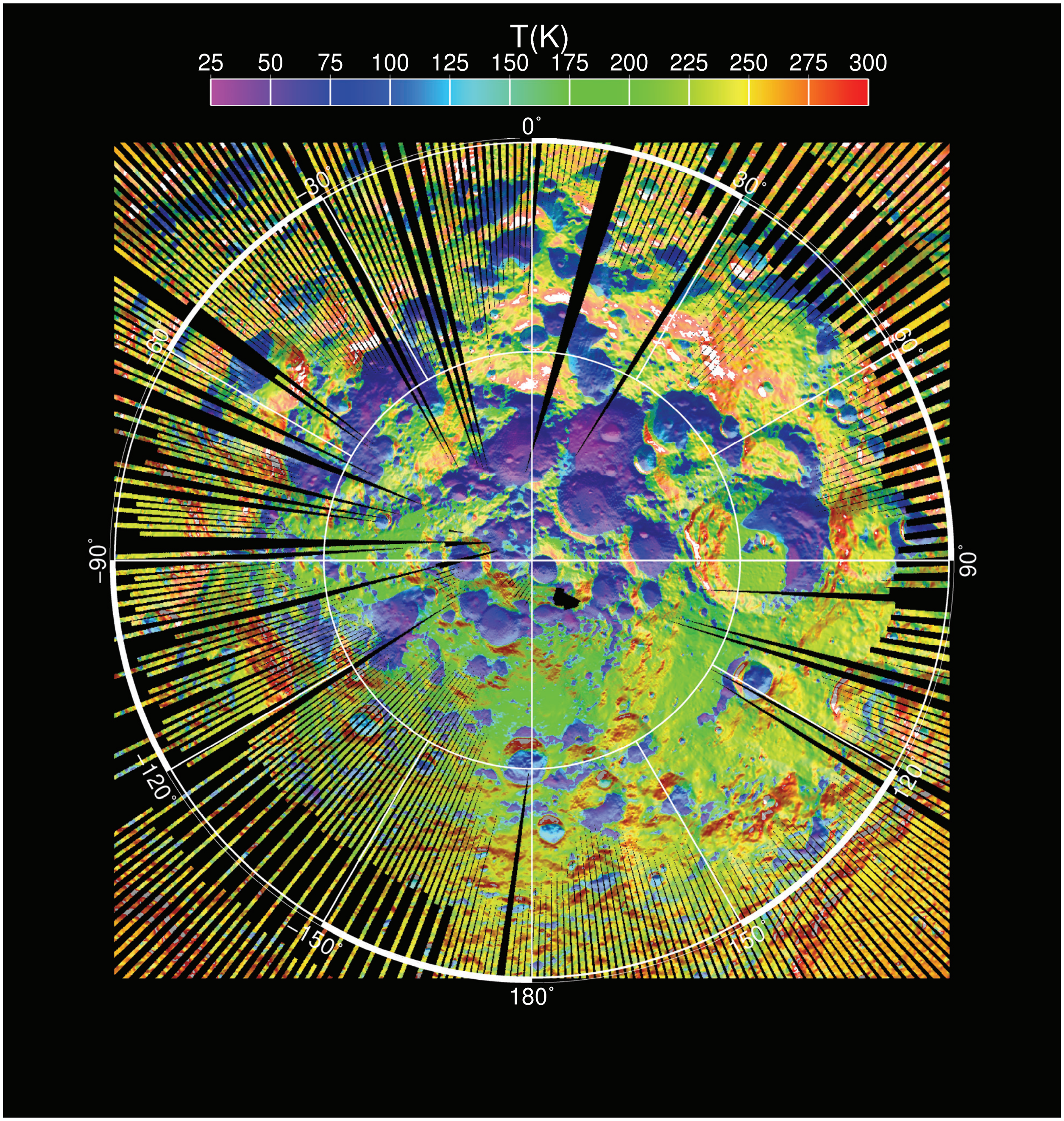

Figure S3-A. Model-calculated daytime surface temperatures at the same locations and times as the Diviner data in Figure 1A.

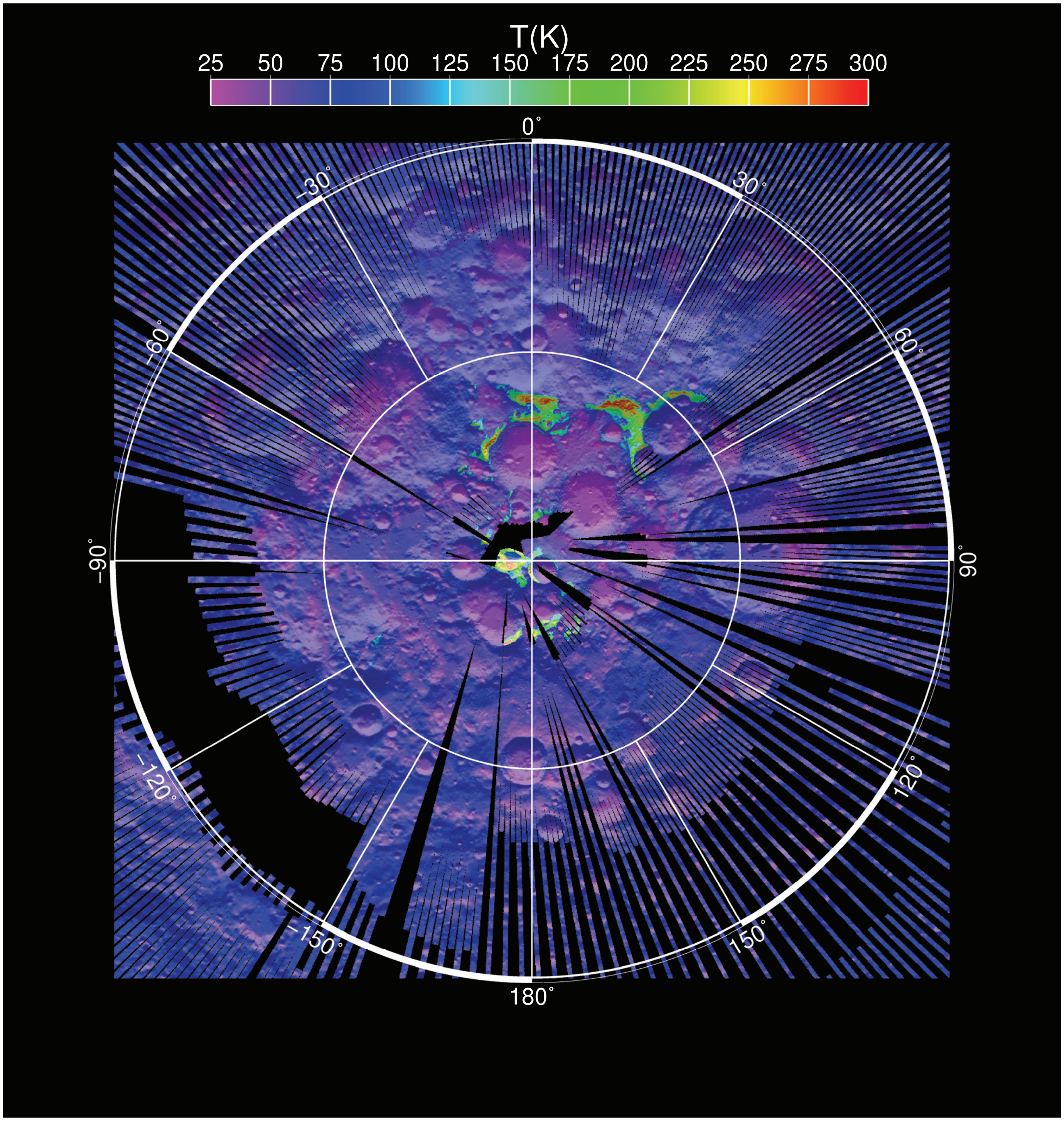

Figure S3-B Model-calculated nighttime surface temperatures at the same locations and times as the Diviner data in Figure 1A.

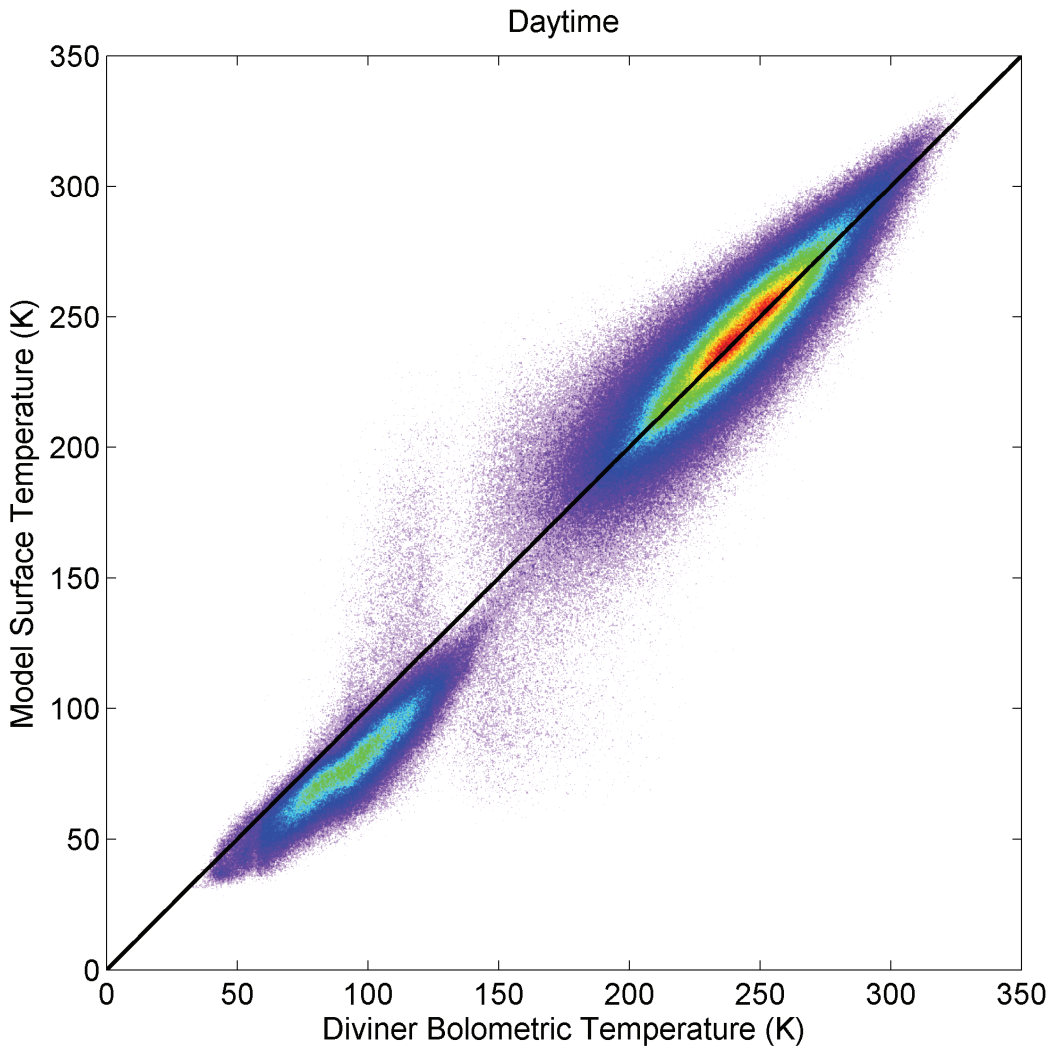

Figure S4-A. Scatter plot of model-calculated daytime surface temperatures vs. measured Diviner bolometric temperatures from the results in Figures 1A and S3A.

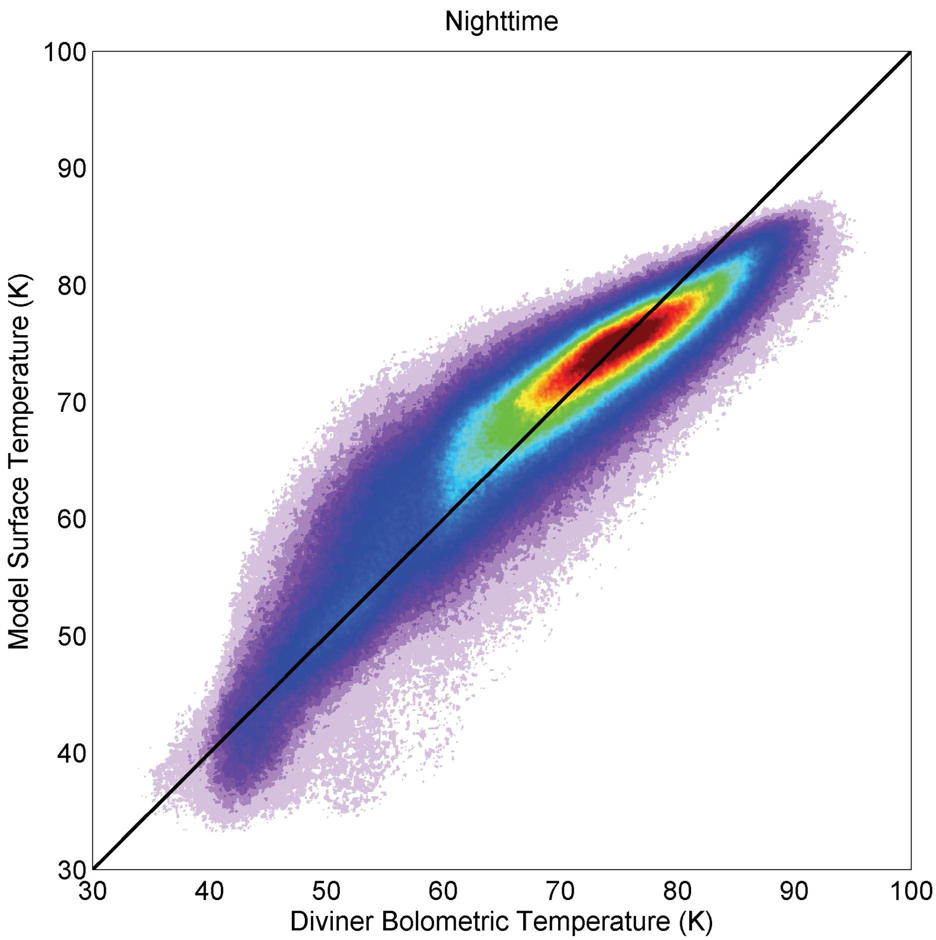

Figure S4-B. Scatter plot of model-calculated nighttime surface temperatures vs measured Diviner bolometric temperatures from the results in Figures 1B and S3-B.

The qualitative and quantitative agreement between the data and models is surprisingly good, given the complete independence of the model from the data, and simplicity and uniformity of the model assumptions. The only significant discrepancy is that model calculated daytime temperatures within shadowed regions with bolometric temperatures of >60K are systematically low by about 15K. The net impact of this discrepancy on model-calculated annual average temperatures is estimated to be less than 7K because most of these craters spend a significant fraction of their time at night, where the agreement between the model and the data is much better. Since the main focus of this paper is to provide a first assessment of the implications of the Diviner temperature measurement on behavior of volatiles, and a discrepancy of this magnitude has no real on the overall conclusions of this work.

Understanding the cause(s) of the discrepancy will be important for future more detailed studies of the thermal behavior and properties and behavior of the polar regions. We have investigated a number of possible explanations, including errors in the model, scattered solar or infrared radiation into the instrument field of view, and unusual albedo or emissivity properties of the crater walls and/or crater floors. The explanation that appears to hold the greatest promise is the directionally anisotropic thermal emission from rough sunlit surfaces (Sarri and Shorthill, 1972; Spencer, 1990). Slopes tilted towards the sun are hotter, and thus emit more infrared radiation than slopes tilted away from the sun. This effect is accounted for in our current model for slopes on scales of 500 meters or larger, but it is not accounted for slopes at smaller scales. The ability of our model to accurately reproduce measured bolometric temperatures for sunlit surfaces at the 500 meter scale is due to the fact that the net effects of small-scale anisotropic thermal emission largely cancel out for nadir viewing geometry at large scales, and that radiative equilibrium dictates that net infrared emission balance net solar absorption. Inside the shadowed regions of partially illuminated craters, infrared radiation emitted by sunlit crater walls is the dominant heating source. In the current model, this radiation is assumed to be emitted in a directionally isotropic manner, whereas in reality, this emission is highly anisotropic – especially at the high emission angles required to reach crater floor regions. We have yet to incorporate this effect into our model to quantify its impact in a detailed manner, but from a qualitative perspective, it appears to be the most promising explanation.

Subsurface Temperatures

When considering the long-term stability of volatiles, it is subsurface temperatures that are of the greatest relevance. Interpreting measurements of surface temperatures in terms of subsurface temperatures is complicated by two factors. The first is that the thermal properties of the lunar regolith are temperature-dependent, which results in annual average temperatures at depth being higher than annual average surface temperatures (Langseth et al 1976). This first effect is most important at higher temperatures due to the non-linear dependence of radiative heat transfer in the regolith with temperature, and it is much less of an issue in the moon's cryogenic regions. The second effect is that temperatures increase with depth due to heat flow from the interior. The lunar heat flow rate at the Apollo 15 and 17 sites has been estimated to be 0.016 to 0.021 W m^{-2} (Langseth et al 1976). The temperature increase with depth depends on the thermal conductivity of the regolith. Figure S5 shows model-calculated minimum, maximum and averaged temperatures as a function of depth for a 500-meter scale region centered on the LCROSS impact site for heat flow rates of 0, 8, 16 and 32 mW m^{-2} using the soil thermal parameters described above.

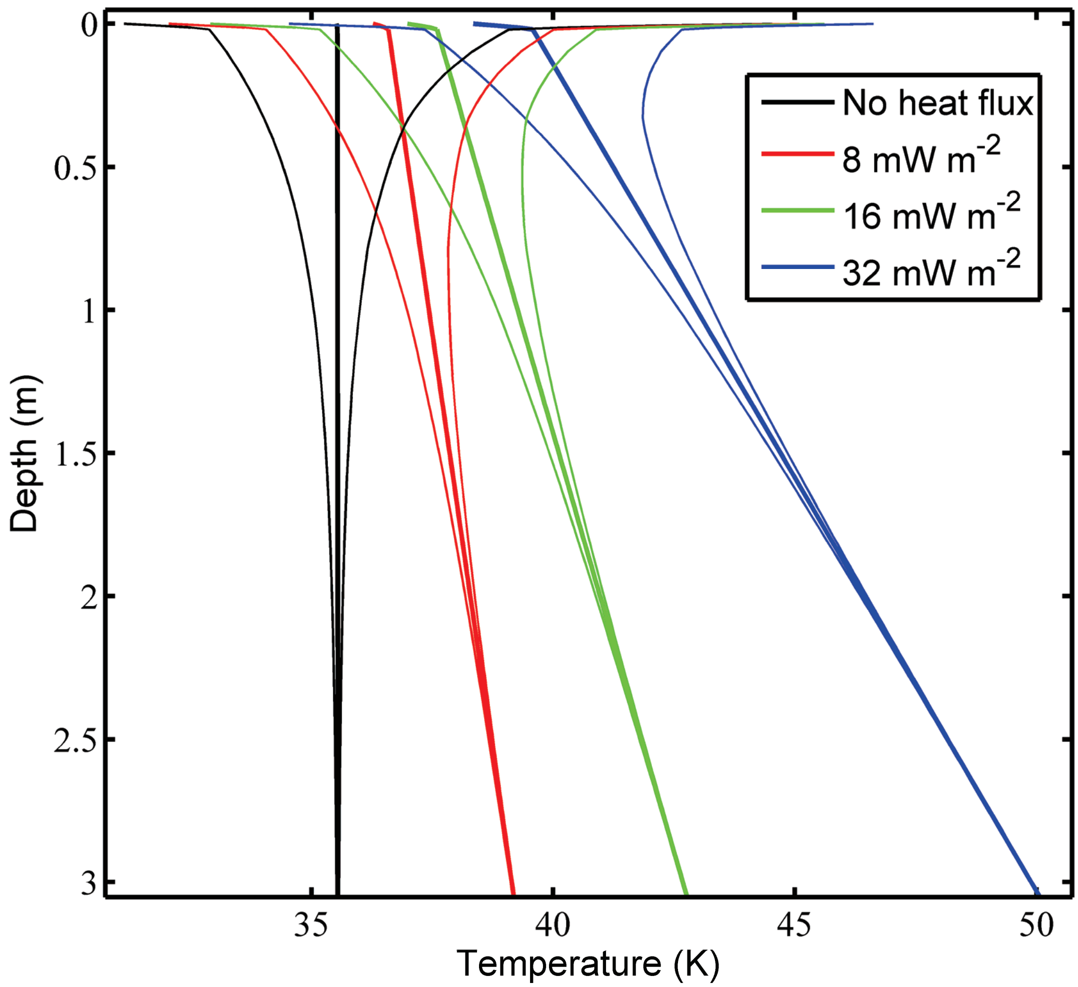

Figure S5. Model-calculated minimum, maximum and averaged temperatures at the LCROSS impact site for heat flow rates of 0, 8, 16 and 32 mW m^{-2}.

The distinct decrease in annual average temperatures in the top 2 cm is due to the effects of temperature-dependent soil conductivity. As a consequence, we use calculated annual average temperatures at 2 cm depth as being more representative of temperatures at greater depth. Our model fits to the Diviner surface temperature observations are most sensitive to the assumed thermal properties in the uppermost ~10 cm of the lunar regolith. The thermophysical properties of the regolith below this level are presently not well constrained, but we would expect that the processes of gravitational compaction and settling that lead to generally increasing regolith density and thermal conductivity with depth as observed at the Apollo sites (Carrier et al., 1991) would similarly affect the regolith in the lunar cold traps. If the subsurface regolith contained substantial quantities of water ice, this would tend to further increase thermal conductivity and decrease the geothermal gradient.

The heat flow rate in the moon's cold traps is highly uncertain, but if it is bounded by the examples shown in Figure S5, then its net effect would be a <6K difference between near-surface annual average temperatures and annual average temperatures at a depth of 2 meters. As illustrated in Figure S5, potential variations in assumed heat flows rates result in a ~4K variations in calculated surface temperatures. It is tempting use model results to deduce heat flow rates in the polar cold traps directly from the Diviner surface temperature observations. However, the dataset used for this study is not optimal for this purpose because it was acquired during a period when surface temperatures in most areas were near their annual maximum values, and the effect of heat flow on surface temperatures is not dominant. With future improvements to the accuracy of the thermal model and Diviner data acquired during winter solstice, we believe it may be possible to put useful limits on heat flow rates at selected locations at both poles.

Volatile Loss Rates

Following the approach of many previous studies, the mass sublimation rate E at temperature T can be expressed as $E = P\sqrt{\frac{\mu}{2\pi RT}}$, where E has units of kg m^{-2} sec^{-1}, P is the saturation vapor pressure, μ is the molecular mass, and R is the ideal gas constant. We define the volatility temperature to be the temperature at which a pure solid would sublimate to space at a rate of 1 mm per billion years. The choice of 1 mm per billion years is arbitrary, but appropriate for situations in which soil volatile mass fractions are small. Adsorbed volatiles can be stable to evaporation at significantly lower than those of the volatility temperature. The volatility temperatures of the compounds shown in Figure 1D were calculated as described in Zhang and Paige (2009) and Zhang and Paige (2010), except for the volatility temperature of water ice which according to the more accurate formulation found in Schorghofer and Taylor (2007), is 101.3K.

The sublimation rates of buried ice deposits are lower than surface sublimation rates due to the diffusive migration of water molecules through the overlying regolith. The same holds true for non-water volatile species. We have calculated the depths to the lunar water ice table as shown in Figure 1D following the approach similar to that described by Schorghofer and Taylor (2007). Since the diffusive mobility of water is a strong function of temperature, we calculate diffusion coefficients and diffusion rates as a function of depth using annual maximum temperature profiles from our thermal model calculations. Starting at the surface, we determine the equilibrium density gradient of water in the regolith required for a constant upward diffusive flux of 1 kg m^{-2} per billion years. We then assume a surface water density of zero and propagate water density profiles downward until they equal a threshold value appropriate to the ice-regolith boundary, at which point the calculated depth to the ice table has been achieved. The major assumptions in this calculation are that the residence times for diffusing molecules on soil surfaces are similar to those for pure solid ice, and that the length-scale for inter-grain diffusion of water is constant with depth. Figure S6 shows the effects of grain length scale on the temperature of the ice table as a function of regolith depth assuming regolith temperatures are equal to the ice table temperature at all depths.

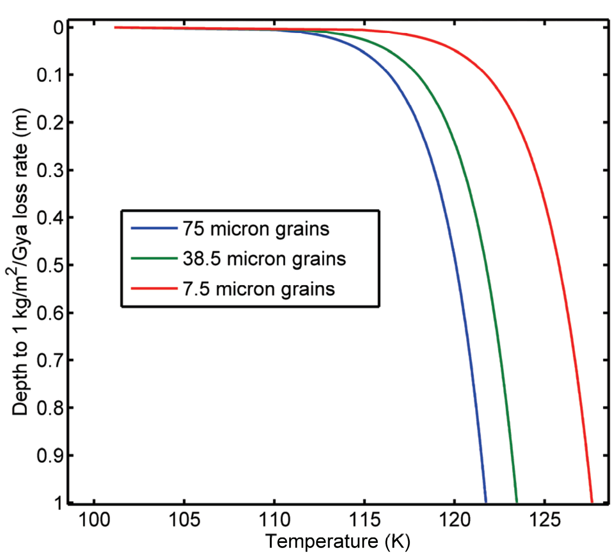

Figure S6. Calculated depths to the lunar ice table including the effects of diffusive water migration through the overlying regolith for three assumed grain-diffusion length scales assuming regolith temperatures are equal to the temperature at the ice table, and constant with depth.

Since annual maximum temperatures increase closer to the surface, diffusion rates also increase closer to the surface, which decreases water density gradients necessary to maintain a constant water vapor flux. The net effect is to move the calculated depth of the ice table to lower levels than if ice table temperatures at all depths are assumed. For the results in Figure 1D, we assume a grain diffusion length scale of 75 microns. Subsurface temperatures are calculated using the same soil thermophysical properties described above, which do not include the potential effects of the presence of ice in the regolith. If substantial quantities of ice were present, it would tend to decrease annual maximum temperatures and move the depth of the ice table closer to the surface (Paige, 1992).

Lunar Spin Pole Evolution

Figure 2C shows changes in the orientation of the damped spin pole of the Moon, relative to its orbit pole. In such a damped state, the spin pole precesses about the orbit pole in the same period as the orbit pole precesses about the ecliptic pole. These changes are mainly driven by changes in the rate at which the lunar orbit pole precesses about the ecliptic pole. The orbit pole precession rate depends on distance from Earth. The oblate Earth influence decreases with distance from Earth, and the solar influence increases with Earth-Moon distance. For details, see Goldriech (1966) and Ward (1975).

We computed diurnal and seasonal variations in the position of the sub-solar point for the model calculations shown in Figure 1B and S7A-D using the following approach. The frequency of the month as calculated from Kepler's 3rd law assuming a 1:1 spin-orbit resonance at the given semimajor axis. The subsolar latitude is sinusoidal in time with an amplitude equal to θ and period equal to the length of the draconic year, where $\omega_{draconic\_year}$= (*2π/precession period* + *2π/365.25 days*). The precession period as a function of semimajor axis is derived by Goldreich (1966) and Touma and Wisdom (1994). The evolution of θ as a function of semimajor axis results from a similar calculation to Ward (1975).

Maps of Annual Average Surface Temperature at θ = 4°, 8°, 12° and 16°

The histograms of calculated annual average temperatures at 2 dm depth in Fig. 2B are derived from the following maps.

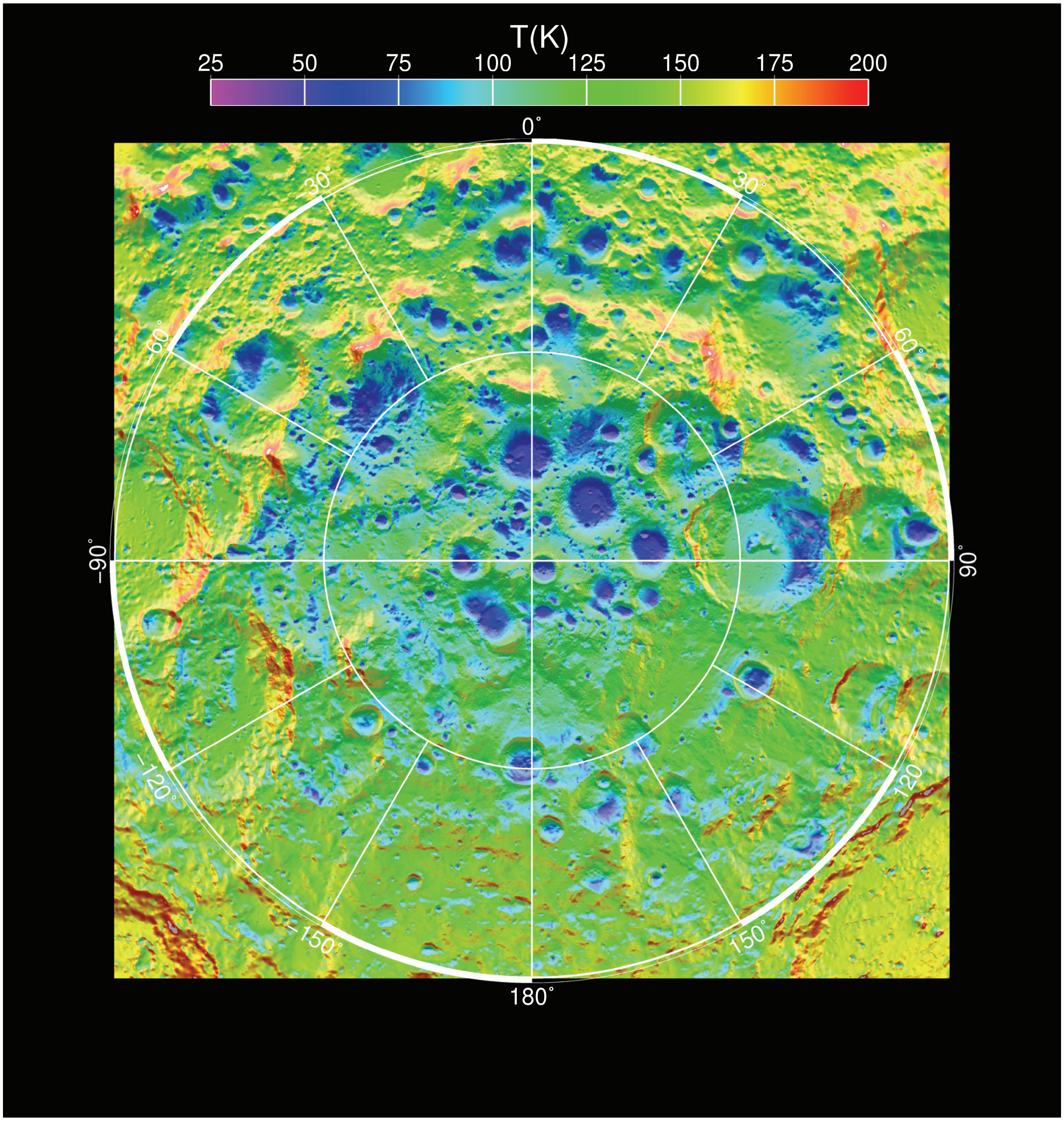

Fig. S7A Calculated annual average surface temperature at 2 cm depth for θ=4°.

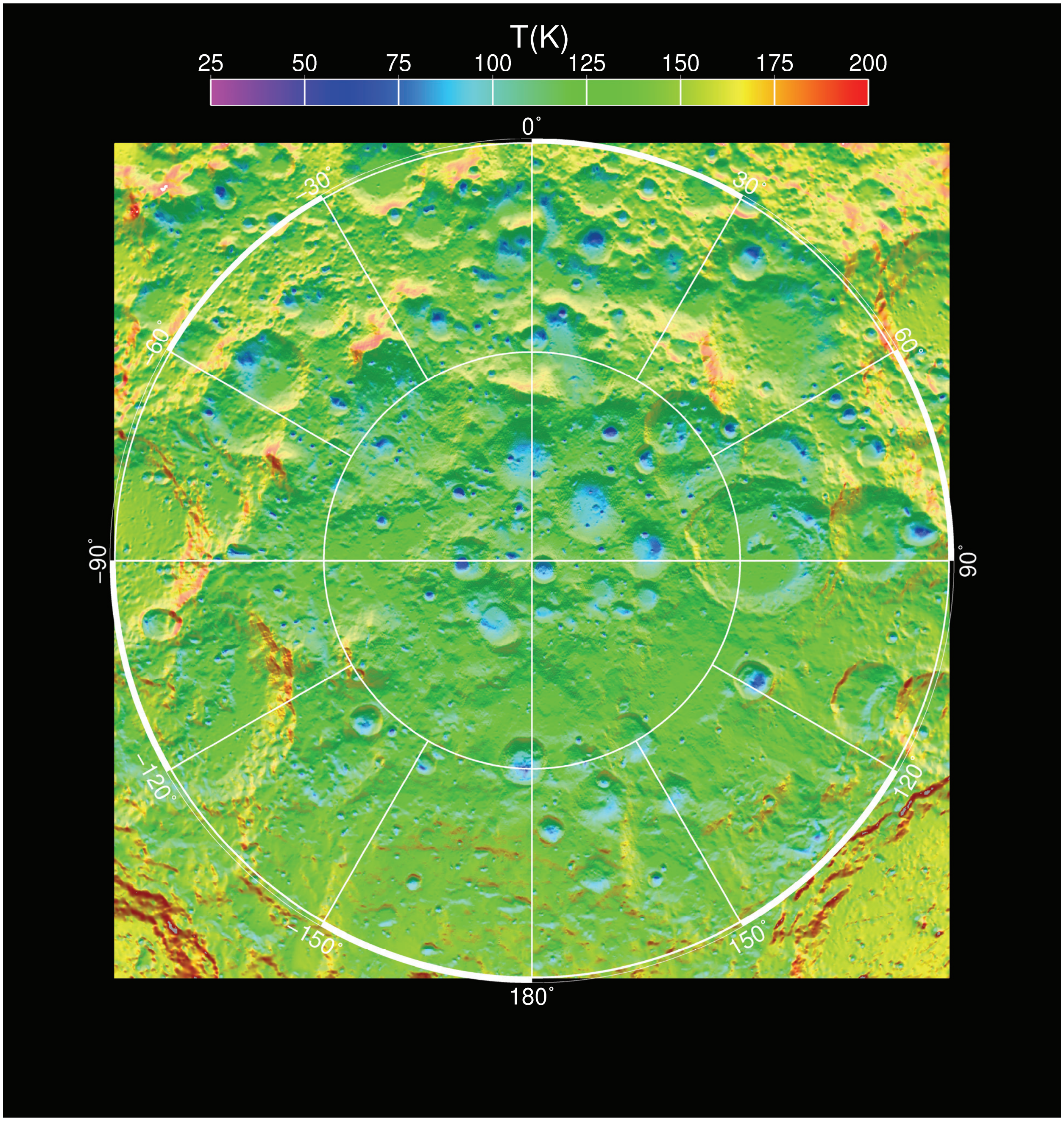

Fig. S7B Calculated annual average surface temperature at 2 cm depth for θ=8°.

431

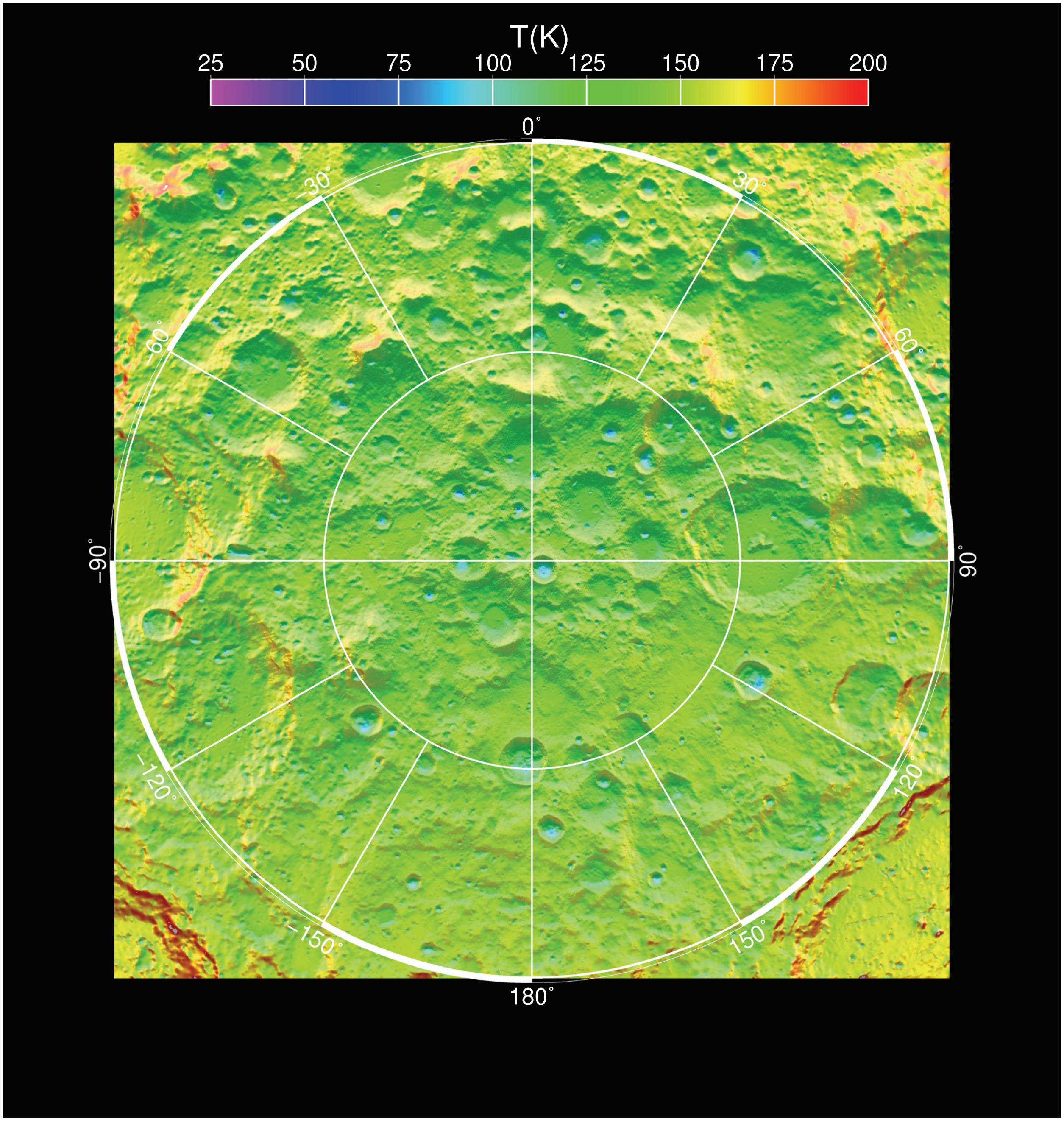

432 **Fig. S7C** Calculated annual average surface temperature at 2 cm depth for θ=12°.

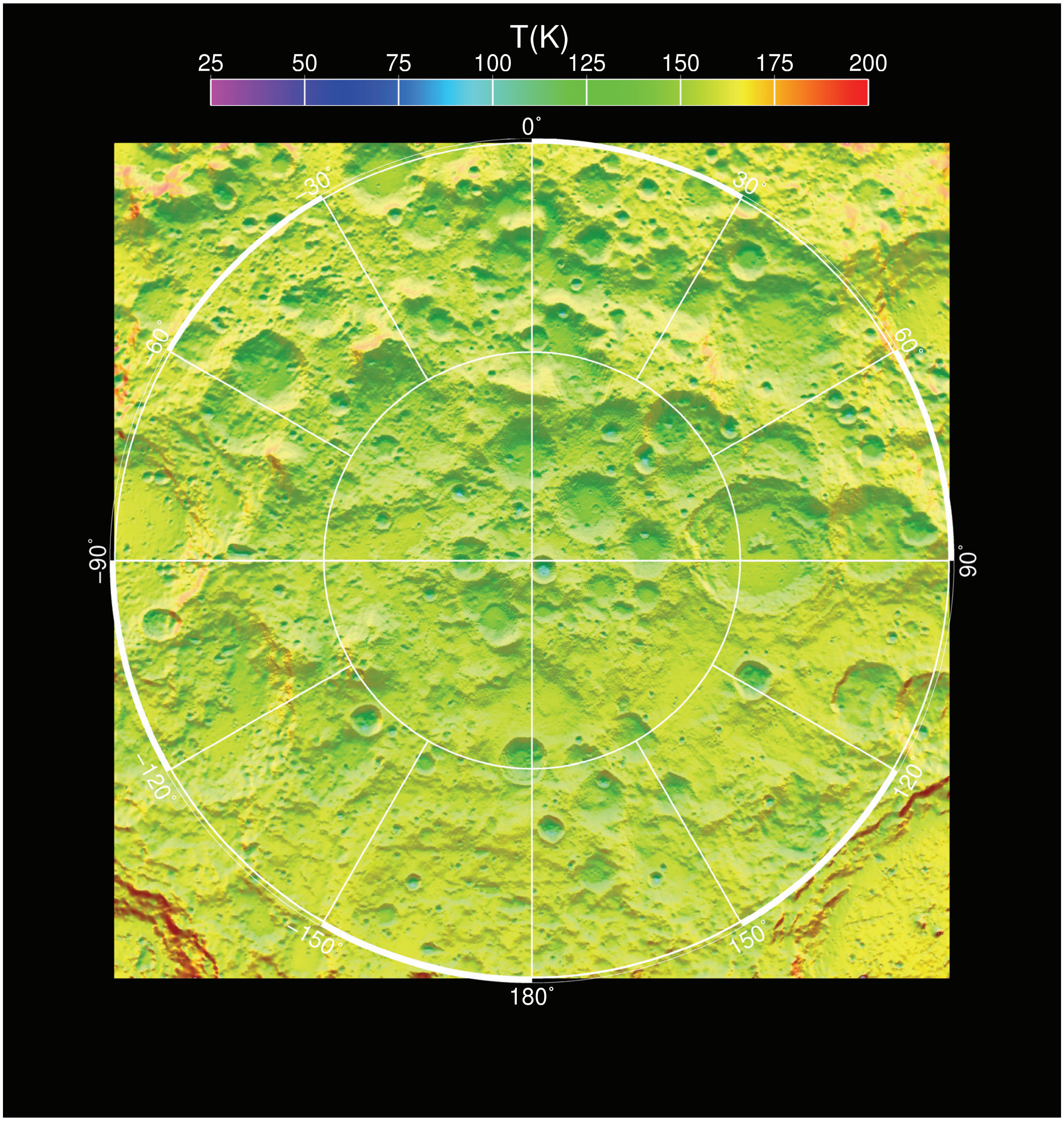

Fig. S7D Calculated annual average surface temperature at 2 cm depth for θ=16°.

The maps show that the coldest areas in the south polar region today are the floors of large impact craters, whereas in the past, the coldest areas were the floors if intermediate-sized impact craters. This transition occurs at θ≈10°. The floors of high-latitude intermediate-sized craters are the moon's oldest volatile cold traps.

References

Araki, H. et. al., *Science* **323**. no. 5916, pp. 897 – 900, DOI: 10.1126/science.1164146.

Carrier, W. D. et al, (1991) Lunar Sourcebook, Cambridge University Press, Chapter 9.

Goldreich, P. (1966) *Rev. of Geophys*., **4**, 411-439.

Isbell, D. et al. (1999) *LPSC* XXX:, Abs. #1812.

Keihm S. and M. g. Langseth (1975) *Icarus* 24, 211-230.

Keihm, S. (1984) Icarus 60, 56S-589;

Langseth, M. G. et al. (1976) *Proc. Lunar Sci. Conf*., 7th, 3143.

Mcewan, A. S. (1996) *LPSC XXVII*, 842.

Negi, B. s. et al (1985) Applied Optics, **24**, No 2.

Paige, D. A. (1992) *Nature* **356**,43.

Paige, D. A. et. al. (2009) *Space Sci. Rev.* DOI: 10.1007/s11214-009-9529-2

Saari, J. M. and R. w. Shorthill (1972) *The Moon* **5**, 161.

Spencer, J. R. (1990) *Icarus* **83**, 27.

Touma, J. and J. Wisdom (1994) *Astronomical Journal*, **108**, 1943-1961.

Vonder Haar T. H. and V.E. Suomi *Science* **163**, 667 (1969)

Ward, W. R. (1975) *Science* **189**, 377.

Zhang, J. A. and D. A. Paige (2009) *Geophys. Res. Lett.*, **36**, L16203, doi:10.1029/2009GL038614.

Zhang J. A. and D. A. Paige, (2010) *Geophys. Res. Lett.*, **37**, L03203, doi:10.1029/2009GL041806.